



Contents lists available at ScienceDirect

Physics of the Earth and Planetary Interiors

journal homepage: www.elsevier.com/locate/pepi



Geodynamo reversal frequency and heterogeneous core–mantle boundary heat flow

Peter L. Olson^{a,*}, Robert S. Coe^b, Peter E. Driscoll^a, Gary A. Glatzmaier^b, Paul H. Roberts^c

^a Department of Earth & Planetary Sciences, Johns Hopkins University, Baltimore, MD 21218, United States

^b Earth and Planetary Sciences Department, University of California, Santa Cruz, CA 95064, United States

^c Institute of Geophysics and Planetary Physics, UCLA, Los Angeles, CA 90095, United States

ARTICLE INFO

Article history:

Received 24 August 2009

Received in revised form 12 February 2010

Accepted 20 February 2010

Edited by: K. Zhang.

Keywords:

Geomagnetic polarity reversals

Core–mantle boundary

Heat flow

Dynamo models

ABSTRACT

We analyze more than two hundred and forty magnetic polarity reversals and excursions over forty million years of time from numerical dynamos with heterogeneous boundary heat flux. Comparisons between a dynamo with uniform boundary heat flux, dynamos with boundary heat flux patterns consisting of a single spherical harmonic, and dynamos with tomographic heat flux patterns proportional to the large-scale lateral variation of seismic shear wave velocity in the lower mantle reveal that boundary heat flux heterogeneity tends to increase the average frequency of polarity reversals relative to uniform boundary conditions, particularly if the heterogeneity increases the average equatorial heat flux. Non-axisymmetric spherical harmonic degree $\ell = 1$ and 2 boundary heterogeneity and the seismically derived tomographic heterogeneity produce comparable reversal and excursion frequencies in our models, suggesting that geomagnetic polarity reversal rates may be relatively insensitive to the non-axisymmetric planform of core–mantle boundary heat flux. In contrast, the average polarity reversal frequency in our models is quite sensitive to the total boundary heat flow and to the total heat flow at the equator, with non-reversing behavior at low heat flow and frequent reversals at high heat flow conditions. Reversal frequency also increases with the amplitude of the boundary heterogeneity, although it is less sensitive to this parameter. Our results suggest that geomagnetic superchrons may correspond to times with reduced core–mantle boundary heat flow, either globally or equatorially, and conversely, periods with high paleomagnetic reversal frequency may correspond to times with increased heat flow at the core–mantle boundary.

© 2010 Elsevier B.V. All rights reserved.

1. Introduction

The durations of individual geomagnetic polarity chrons are highly irregular, according to the paleomagnetic record, but when averaged over millions of years, there is evidence for more regular variations. Over the past 120 Myr the average frequency of geomagnetic polarity reversals shows an overall increase with time, from zero reversals during the Cretaceous Normal Superchron (CNS) from 120 to 83 Ma, to about 4 Myr^{-1} in the past 5 Myr (Cande and Kent, 1995). The paleomagnetic record also shows a progressive decrease in average reversal frequency prior to the CNS (McFadden and Merrill, 2000; Constable, 2003; Lowrie and Kent, 2004), although the actual onset of the CNS may have been more abrupt than gradual (Hulot and Gallet, 2003). The CNS, the Kiaman Reversed Superchron at 310–260 Ma (Opdyke and Channell, 1996), and a possible third Phanerozoic superchron around 490–460 Ma

(Pavlov and Gallet, 2005) imply approximate 40 Myr duration and 200 Myr recurrence time scales for geodynamo fluctuations. Both of these are extremely long compared to the known time scales for dynamical processes in the outer core, where the convective turnover time is estimated to be a few centuries (Hongre et al., 1998) and the dipole free decay time is about 20 kyr (Moffatt, 1978). They are, however, far shorter than the core evolutionary time scale as measured by the age of the inner core, which is estimated to be about 1–2 Ga (Labrosse et al., 2001).

Several interpretations have been proposed for these long-term variations in polarity reversal frequency. One interpretation is that reversals are random events and the geodynamo processes that cause them are statistically time invariant. According to this interpretation, superchrons represent the low frequency tail of a continuous distribution of polarity chron lengths (Jonkers, 2007; Ryan and Sarson, 2007). A second interpretation assumes that the underlying geodynamo processes are non-stationary in time, although individual polarity reversals are essentially random events. According to this interpretation, the non-stationary geodynamo behavior is driven by low frequency geodynamic vari-

* Corresponding author.

E-mail address: olson@jhu.edu (P.L. Olson).

ability, such as secular changes in Earth's rotation (Driscoll and Olson, 2009a), and more importantly, changes in the heat flux at the core–mantle boundary (Courtillet and Besse, 1987; Larson and Olson, 1991; Gallet and Hulot, 1997; Courtillet and Olson, 2007). A third alternative suggested by Hulot and Gallet (2003) is that the geodynamo flips between reversing and non-reversing states by internal nonlinear processes, with no changes in boundary conditions required.

This paper focuses on the role of boundary heat flux heterogeneity in controlling polarity reversal rates. The heat flux at the core–mantle boundary (CMB) is governed by mantle convection and is therefore laterally heterogeneous and also time dependent. On a global scale, the lateral heterogeneity of the CMB heat flux probably has a large spherical harmonic degree $\ell = 2$ component, consistent with the dominant $\ell = 2$ pattern of seismic heterogeneity in the present-day lower mantle (Dziewonski, 1984; Masters et al., 2000). It is unclear how much this low degree pattern has changed with time, although 3D spherical models of mantle convection suggest that the dominant spherical harmonic in mantle convection may alternate between non-axisymmetric $\ell = 1$ and $\ell = 2$ (Yoshida, 2008), with non-axisymmetric $\ell = 1$ mantle flow corresponding to supercontinent aggregation and non-axisymmetric $\ell = 2$ dominating after supercontinent breakup (Zhong et al., 2007).

Numerical dynamos show that long wavelength heat flux heterogeneity at the CMB induces departures from axisymmetry in the time-average structure of the geomagnetic field (Olson and Christensen, 2002; Christensen and Olson, 2003; Willis et al., 2007; Aubert et al., 2008) and preferred paths for the geomagnetic pole during polarity transitions (Coe et al., 2000; Kutzner and Christensen, 2004). In addition, laboratory experiments (Sumita and Olson, 2002) and frozen flux models of geomagnetic secular variation (Amit et al., 2008) show that heat flux heterogeneity on the CMB alters the pattern and scale of core flow. Evidence for this thermal coupling between the core and mantle is seen in the correlation between the non-axisymmetric part of the present-day geomagnetic field on the CMB and the pattern of lower mantle seismic heterogeneity (Gubbins et al., 2007).

The first systematic investigation of how thermal heterogeneity in the lower mantle affects geomagnetic polarity reversal frequency was made by Glatzmaier et al. (1999), hereafter abbreviated GCHR99. They compared numerical dynamos driven by eight distinct patterns of core–mantle boundary heat flux, including a uniform case, six cases with patterns consisting of a single spherical harmonic, and one case with CMB heat flux proportional to lower mantle seismic shear wave heterogeneity, the boundary condition that we refer to in this paper as tomographic forcing. In all these cases, the average CMB heat flux and the amplitude of its lateral heterogeneity were the same. Simulation times in the GCHR99 study were limited to 300 kyr or less and in some cases only a few reversals were recorded. GCHR99 nevertheless found clear evidence that boundary heat flux heterogeneity tends to weaken and destabilize the axial dipole and increase reversal frequency relative to the homogeneous situation, except for two models with axisymmetric spherical harmonic degree $\ell = 2$ and $\ell = 4$ boundary heat flux patterns that produced stronger and more stable axial dipole fields. Later, Coe and Glatzmaier (2006) proposed that the variety of reversal frequencies in these models could be explained in terms of the amount of equatorial symmetry in their time-averaged magnetic fields on the CMB.

Another systematic study by Kutzner and Christensen (2004), hereafter abbreviated KC04, examined numerical dynamos driven primarily by compositional buoyancy but with heterogeneous outer boundary heat flux included. KC04 found comparable reversal frequencies in otherwise similar dynamos with uniform, tomographic, and spherical harmonic degree and order $\ell = m = 2$

harmonic forcings. They found higher reversal frequencies in dynamos with positive axisymmetric equatorial heat flux anomalies, including a model with the $\ell = 4$ pattern that GCHR99 found to be stabilizing, and relatively lower reversal frequencies in dynamos with negative axisymmetric equatorial heat flux anomalies. They also examined reversal sensitivity to the amplitude of the heterogeneous forcing, but found no significant differences in reversal frequency with this parameter.

In addition to CMB heat flux pattern, it has been proposed that the total CMB heat flow exerts control on geomagnetic polarity reversal rates (Courtillet and Olson, 2007). Although this property has received less attention than CMB heat flux heterogeneity, time variations in the total core heat flow are expected, based on our current understanding of mantle and core dynamics. Thermal evolution models incorporating mantle convection predict small variations in total CMB heat flow and inner-core growth rate on 200–400 Myr time scales (Nakagawa and Tackley, 2004) and dynamo models have demonstrated that the reversal frequency is sensitive to small changes in these parameters (Kutzner and Christensen, 2002; Driscoll and Olson, 2009b).

Here we examine the control of geomagnetic reversal frequency by CMB heat flux heterogeneity using numerical dynamos with longer run times and larger numbers of reversals and excursions than in the GCHR99 and KC04 studies. We compare dynamos with boundary heat flux patterns consisting of individual spherical harmonics, as well as dynamos with tomographic forcing in which we vary the amplitude of the mean boundary heat flux and the amplitude of its lateral heterogeneity. Our results indicate that CMB heat flux heterogeneity increases polarity reversal frequency in most cases. More importantly, we find a strong sensitivity to the average heat flux on the CMB, including the average heat flux in the equatorial region. Increases or decreases of these properties can result in large increases or decreases, respectively, in the reversal frequency.

2. Core–mantle boundary heat flux

Lower mantle thermal heterogeneity inferred from global seismic tomography (Trampert et al., 2004), seismic body waves (Van der Hilst et al., 2007; Lay et al., 2008), results from spherical mantle convection calculations (Nakagawa and Tackley, 2008), and laboratory convection experiments (Gonnermann et al., 2004) all point to global-scale lateral temperature variations in the lower mantle of several hundred degrees, implying that the heat flux on the CMB must also be laterally heterogeneous. However, the total heat flow from the core and its spatial and temporal variations are poorly constrained, due to uncertainties in both the thermal gradient and thermal conductivity in the D'' -region. Estimates for the present-day total core heat flow range from around 4 TW to as high as 15 TW (Lay et al., 2008), which correspond to average CMB heat fluxes \bar{q} near 26 and 98 mW/m², respectively. Lateral heat flux variations on the CMB are even less well-constrained. Seismic reflectors above the CMB interpreted as post-perovskite phase transitions yield estimates of $|\delta q| = 25\text{--}45$ mW/m² for amplitude of the variation (Lay et al., 2006; Van der Hilst et al., 2007). Spherical mantle convection calculations typically give relative variations of $|\delta q|/\bar{q} \simeq 0.5$ (Nakagawa and Tackley, 2008), while laboratory experiments on heterogeneous convection on both the mantle side (Gonnermann et al., 2004) and on the core side of the CMB (Sumita and Olson, 2002) suggest somewhat smaller ratios, $|\delta q|/\bar{q} \simeq 0.2$.

A widely used method for representing the large-scale planform of CMB heat flux in numerical dynamos is to assume that the lateral variations in CMB heat flux are linearly proportional to the lateral variations in seismic shear wave velocity in the lower mantle (see GCHR99; KC04; Olson and Christensen, 2002; Christensen

and Olson, 2003; Aubert et al., 2008), so that

$$\frac{\delta q}{\bar{q}} \propto \frac{\delta V_s}{\bar{V}_s} \quad (1)$$

where \bar{V}_s and δV_s are, respectively, the spherically symmetric and lateral variations of shear wave velocity at some depth in the lower mantle, typically near the top of the D'' -region about 200 km above the CMB. The physical justification for (1) is that V_s varies inversely with temperature in the lower mantle (Trampert et al., 2004), so at those places above the CMB where V_s is larger than average, the radial thermal gradients are larger than average and therefore the CMB heat flux is higher than average. The proportionality coefficient in (1) can be estimated from mineralogical properties of lower mantle compounds, or alternatively, from the results of mantle convection models. Nakagawa and Tackley (2008) have shown that a simple linear relationship like (1) with a proportionality factor of 25–50 is a good approximation for purely thermal mantle convection, and even though it does not take compositional or phase heterogeneity into account, piece-wise linear relationships like (1) still apply over restricted ranges of $\delta V_s/\bar{V}_s$ where the post-perovskite phase change and chemical heterogeneity are present in the D'' -region. For dynamos with tomographic forcing in this study, we simply assume that a single relationship like (1) holds everywhere on the CMB.

3. Dynamo model parameters and boundary conditions

The dynamo model solves the Boussinesq equations for conservation of mass, momentum, energy and magnetic field together with the magnetic induction equation for an electrically conducting, rotating, Newtonian viscous fluid in a spherical shell with radial gravity. Density perturbations, relative to a constant background density, drive convection in the model's liquid outer core through a combination of thermal buoyancy derived from the heat flow at the CMB and at the inner-core boundary (ICB), as well as compositional buoyancy derived from the continuous enrichment of light elements in the outer core (including Si, S, and O; see Alfe et al., 2000) that accompanies inner-core solidification (Gubbins et al., 2004).

A convenient way to represent this thermo-chemical convection is to combine temperature and the light element concentration into a single hybrid co-density variable C (Braginsky and Roberts, 1995), defined as

$$C = \alpha T + \beta \chi \quad (2)$$

where T is temperature, χ is light element concentration or mixing ratio (defined as the ratio of the local light element density divided by the reference state density ρ_o) and

$$(\alpha, \beta) = -\frac{1}{\rho_o} \left(\frac{\partial \rho}{\partial T}, \frac{\partial \rho}{\partial \chi} \right) \quad (3)$$

are the expansion coefficients for temperature and composition, respectively, ρ is total density, and the subscript o denotes outer core average. Note that a positive C means a negative density perturbation and therefore an upward buoyancy force. Assuming that T and χ have the same effective diffusivities, a simplifying assumption that is commonly invoked to model multi-constituent turbulent flows, the transport-diffusion equations for T and χ can be combined into a single equation for C (Braginsky and Roberts, 1995; Kutzner and Christensen, 2000). If we scale C using the average rate of light element enrichment in the fluid $\dot{\chi}_o$ (here assumed fixed), then the Rayleigh number for compositional convection can be written (Driscoll and Olson, 2009a)

$$Ra = \frac{\beta g_c D^5 \dot{\chi}_o}{\kappa \nu^2} \quad (4)$$

where g_c is gravity at the outer boundary, $D = r_c - r_i$ is fluid shell thickness, r_c and r_i are outer and inner radii, respectively, κ is the diffusivity of the co-density, and ν is the kinematic viscosity of the fluid.

Heterogeneous thermal forcing requires special consideration of the boundary conditions on C . At the outer boundary we specify the amplitude and the pattern of the heat flux and set the light element flux to zero, which provides a flux condition on C in terms of the boundary heat flux alone. At the Earth's inner-core boundary, the fluxes of heat and light elements are thermodynamically coupled through the growth rate of the solid inner core (Braginsky and Roberts, 1995). For modeling purposes however, KC04 showed that fixing χ and T at constant values on the inner boundary amounts to a fixed value of C there, and $\dot{\chi}_o$ enters as a uniform volumetric sink term in the co-density equation for the fluid. Other volumetric terms appearing in the co-density equation from radioactive heating, sensible heat loss, and curvature of the adiabat (see Jones, 2007) are ignored here.

The Boussinesq approximation allows us to interpret the outer boundary co-density flux in the model as equivalent to the CMB heat flux q minus the heat flux conducted down the core adiabatic gradient q_a . The total flux of C at the inner boundary of the model (corresponding to superadiabatic heat and light element release in the core) balances the total flux of C at the outer boundary of the model (corresponding to superadiabatic heat loss from the core) plus the total strength of the volumetric sink term of the model (corresponding to light element enrichment in the outer core.) In terms of this co-density formulation, the boundary conditions on C are

$$C(r_i) = C_i \quad (5)$$

at the inner boundary and

$$\frac{\partial C}{\partial r}(r_c) = -\frac{\alpha}{k} q_c \quad (6)$$

at the outer boundary, where k is the thermal conductivity of the fluid and q_c is the boundary heat flux. For application to the core, we use

$$q_c = q - q_a \quad (7)$$

According to (7), $q_c > 0$ in (6) corresponds to a superadiabatic core heat flux and a convectively unstable thermal stratification below the CMB, while $q_c < 0$ corresponds to subadiabatic core heat flux and a convectively stable thermal stratification below the CMB.

We use two dimensionless parameters to characterize the CMB heat flux and its heterogeneity. Writing the superadiabatic heat flux in (6) as the sum of a spherical average (denoted by an overbar) and a laterally varying part (denoted by δ),

$$q_c = \bar{q}_c + \delta q_c(\theta, \phi) \quad (8)$$

where (θ, ϕ) are colatitude and longitude, respectively, the dimensionless parameters are \bar{f}_c and δf_c , defined as

$$\bar{f}_c = \frac{\alpha \kappa \bar{q}_c}{k D \dot{\chi}_o} \quad (9)$$

and

$$\delta f_c = \frac{\alpha \kappa |\delta q_c|}{k D \dot{\chi}_o} \quad (10)$$

where $|\delta q_c|$ denotes the amplitude variation of δq_c . Note that these parameters are proportional to the ratio of the superadiabatic heat flux on the CMB to the total volumetric sink rate of co-density within the fluid core. The parameter \bar{f}_c denotes the contribution to the buoyancy in the outer core due to the superadiabatic heat flux averaged over the CMB, whereas δf_c denotes the contribution to the buoyancy in the outer core due to the CMB heat flux heterogeneity.

The parameter $\delta f_c / \bar{f}_c$ is equivalent to the boundary heterogeneity parameter used by Olson and Christensen (2002) and Aubert et al. (2008) in their studies of dynamos with tomographic forcing, whereas δf_c is the parameter used by KC04 to characterize their dynamos with heterogeneous thermal boundary forcing. The other model boundary conditions are no slip and electrically insulating at both the inner and outer boundaries.

Other dimensionless control parameters for the dynamo model include the Ekman, Prandtl, and magnetic Prandtl numbers and the radius ratio, defined as

$$E = \frac{\nu}{\Omega D^2}, \quad (11)$$

$$Pr = \frac{\nu}{\kappa}, \quad (12)$$

$$Pm = \frac{\nu}{\eta}, \quad (13)$$

and

$$R = \frac{r_i}{r_c} \quad (14)$$

respectively, where Ω is angular velocity of rotation and η is magnetic diffusivity.

Important output parameters include magnetic field properties such as B_{rms}^v , the rms field intensity in the fluid volume, B_{rms} , the rms field intensity on the outer boundary, B_d , the rms dipole field intensity on the outer boundary, B_a , the axial dipole field intensity on the outer boundary, the rms fluid velocity in the fluid, u_{rms} , and the average frequencies of polarity reversals and excursions. We report these parameters in dimensionless form. We use the shell thickness D as the length scale (with $R=0.35$) and η/D for the velocity scale, so that our dimensionless velocities are equivalent to $Rm = u_{rms}D/\eta$, the rms magnetic Reynolds number of the convection. We use $(\rho_0\Omega/\sigma)^{1/2}$, where σ is the electrical conductivity, to non-dimensionalize the magnetic field intensity. Time variations in these properties and the rates of reversals and excursions are also given in non-dimensional form. Our unit of time τ is the e-fold free decay time of a dipole field in a uniformly conducting sphere with radius r_c , given by

$$\tau = \frac{r_c^2}{\pi^2\eta} \quad (15)$$

For the core, $\tau \simeq 20$ kyr. We analyze dynamos with $Pr = 1$ for the Prandtl number, $Pm = 20$ for the magnetic Prandtl number, $E = 6.5 \times 10^{-3}$ for the Ekman number, and $Ra = 2.8 \times 10^4$ for the Rayleigh number. Although not realistic for the geodynamo, the large magnetic Prandtl number provides a large magnetic Reynolds number at modest Ra , which ensures strong magnetic field induction, a large Lorentz force, and according to Kutzner and Christensen (2002), favors a dipole-dominated magnetic field at stable polarity times. Driscoll and Olson (2009b) found $Ra_{crit} \simeq 10^4$ for the Rayleigh number at convective onset for these parameters.

The convective magnetohydrodynamic (MHD) dynamo code MAG used in this study (available at www.geodynamics.org) is a Boussinesq version of the anelastic dynamo code described in Glatzmaier (1984) and in Glatzmaier and Roberts (1996). It employs a fully spectral method with variables expanded in spherical harmonics to describe their horizontal structures and in Chebyshev polynomials for their radial structures. A spectral transform method is used to compute the nonlinear terms at each numerical time step. The time integration treats the linear terms with an implicit Crank–Nicholson scheme and the nonlinear and Coriolis terms with an explicit Adams–Bashforth scheme. It has been previously benchmarked against standard dynamo solutions (Christensen et al., 2001). In this study we use a relatively coarse spatial resolution: 25 radial grid levels, 48 latitudinal levels and

96 longitudinal levels and, in spectral space, 23 Chebyshev polynomials and all spherical harmonics up to degree ℓ_{max} and order $m_{max} = 31$. For the tomographic forcing function $\delta q(\theta, \phi)$ we use (1) with the Masters et al. (2000) lower mantle shear velocity heterogeneity model at 200 km above the CMB and truncated at spherical harmonic degree and order $\ell_{CMB} = m_{CMB} = 4$.

In our simulations we distinguish reversals from excursions on the basis of event duration. Reversals are defined as events where the dipole axis crosses the equator and then stabilizes in the opposite hemisphere for at least one dipole free decay time. Excursions are often more ambiguous to define precisely (Gubbins, 1999). In particular, our dynamos include many dipole collapse events in which the dipole field becomes quite weak for a time, much like the dipole lows in the marine paleomagnetic intensity record (Valet et al., 2005). However, some of these model dipole collapse events do not involve major departures of the dipole axis from its time average high-latitude position, and would not necessarily qualify as excursions. In order to filter such events out, we only count them as excursions if the dipole axis crosses the equator and then returns to its original hemisphere within one dipole free decay time, without stabilizing in the opposite hemisphere. This criterion is basically consistent with Valet et al. (2008), who define geomagnetic excursions as low dipole field configurations that include an aborted (i.e., temporary) polarity change.

Long-lasting transition fields provide another source of ambiguity. Most of the events in this study involve the transition from a dipole-dominant field configuration to a multipolar field configuration, where the dipole field is secondary in strength to the non-dipole field. In simple reversals and excursions the dynamo remains in the multipolar configuration for a short time only, and in these cases it is relatively straightforward to distinguish excursions from reversals. If the dynamo lingers in the multipolar configuration, however, the position of the dipole axis varies wildly and may cross the equator often in a short interval of time. Counting each of these axis crossings as an individual excursion seems problematic, so to minimize over-counting complex events we simply treated the entire event as one reversal or excursion, depending on its duration.

4. Dynamo model scaling

Application of numerical dynamos to the geodynamo requires judicious extrapolation of all the model variables to Earth's core conditions, and furthermore, dynamo modeling necessarily involves a tradeoff between temporal coverage and spatial resolution (Christensen and Wicht, 2007). Fine spatial resolution allows a closer approach to the extremely small values of the control parameters E and Pm used to characterize convection in the Earth's core (Jones, 2007), and dynamo models with small Ekman and Prandtl numbers (see Takahashi et al., 2005, 2007, 2008; Kageyama et al., 2008, for examples) have more of the energetic small scale motions that are generally considered to be an important property of convection in the core (Glatzmaier, 2002). However, these models are restricted to short run times. For example, the very high spatial resolution numerical dynamos recently reported by Kageyama et al. (2008) at $E \simeq 10^{-7}$ were run for less than one magnetic free decay time. At the opposite extreme, Wicht et al. (2008), hereafter referred to as WSH08, have analyzed a 160 Myr dynamo simulation with $E \simeq 10^{-2}$, a low Ra and a large Pm that reversed polarity more than 100 times. Our numerical dynamos are close in parameter space to WSH08. We have run several of our dynamos in excess of 250τ , corresponding to 5 Myr of paleomagnetic time. Although our simulations are shorter than WSH08, we nevertheless capture an average of 15 reversals and excursions per case.

Although it is not possible to use realistic Ekman and Rayleigh numbers in numerical dynamos, it is possible to represent certain aspects of convection in the core by properly choosing their ratio. A dimensionless parameter that is often used to control the relative strengths of buoyancy and rotation in dynamo models is the convective Rossby number Ro_c , which can be written in terms of our parameters as

$$Ro_c = EPr^{-1/3} Ra^{1/3} \quad (16)$$

The convective Rossby number (16) is useful in this context because it is independent of the highly uncertain diffusivities. In addition, Christensen and Aubert (2006), Olson and Christensen (2006) have shown that several output properties of convection-driven dynamos, including magnetic field intensity and fluid velocity, can be scaled in terms of this parameter. For the dynamo models in our study, $Ro_c \simeq 0.2$, whereas $Ro_c \simeq 0.006$ in GCHR99.

There are multiple ways to define time in dynamo modeling, each with its advantages and drawbacks. In choosing to measure time based on the Earth's magnetic dipole diffusion time, and using Prandtl numbers of unity or larger along with an Ekman number of 6.5×10^{-3} , the rotation period in our simulations is several orders of magnitude too long, approximately 165 Earth years. A more realistic Ekman number of, say, $E = 10^{-9}$ would allow both the correct magnetic diffusion time and correct rotation period while having (turbulent) Prandtl numbers no larger than unity (Glatzmaier, 2002). Ultimately it is important for models to have both of these times correct, because the Lorentz and the Coriolis forces are critical in the geodynamo process. Unfortunately, no simulation has been able to reach this Ekman number, not for a short amount of simulated time and certainly not for millions of years. So for now, magnetic diffusion time scaling remains the best way for geodynamo modelers to cope with the existing computational limitations, even if it obscures important differences between the models and the geodynamo.

Some simulations (e.g., GCHR99) have used both the correct magnetic diffusion time and the correct rotation period, but at the price of having large Prandtl numbers, i.e., the viscous diffusivity was a couple orders of magnitude larger than the magnetic, thermal and compositional diffusivities, which also is unrealistic. The advantage of this approach though is that realistic values for fluid velocity and magnetic field produce realistic amplitudes for both the Lorentz and Coriolis forces, which are still larger than the viscous forces. The disadvantage is that this approach requires a numerical time step that is at least 10 times smaller than the rotation period to avoid a numerical instability related to inertial oscillations. This time step constraint has been of little concern for those studies that have chosen to use a very long rotation period, but for those that employ a one-day rotation period, it makes multi-million-year simulations prohibitively expensive. That is the reason GCHR99 treated the Coriolis terms implicitly, which avoided this constraint and allowed time steps of order 15 days. Although an implicit treatment of the Coriolis terms requires a more complicated numerical method and more memory for a given spatial resolution, it may be worth while if maintaining the relative significance of the Coriolis force is critical.

The above discussion concerns the model input parameters. Model output parameters also have to be scaled to the core. For the convective velocity, the usual scaling is based on the magnetic Reynolds number of the flow, which is of order several hundred in the core. Our numerical dynamo models are at the low end of this range. Scaling of the numerical dynamo model magnetic fields to the core is more contentious. It is often assumed that the Elsasser number for the core is of order unity, which would mean that our model non-dimensional magnetic fields should also be of order unity. However, Christensen and Aubert (2006) have argued that a different magnetic scaling is appropriate for convection-driven

dynamos, one that depends on the convective buoyancy flux and is based on a parameter like (16). Christensen and Aubert (2006), Olson and Christensen (2006), Driscoll and Olson (2009b) have shown that a scaling relation of the form

$$B_d^{cmb} = \gamma(\rho_o \mu_o)^{1/2} (g_c \beta R (\dot{\chi}_o - \dot{\chi}_{cr}) D^2)^{1/3} \quad (17)$$

is applicable for the dipole field strength in these compositionally driven dynamos. Here B_d^{cmb} denotes the time average rms geomagnetic dipole field strength on the CMB in Tesla, μ_o is magnetic permeability, $\dot{\chi}_{cr}$ is the critical rate of light element increase for convective onset in the outer core and γ is a proportionality coefficient. For application to the geodynamo we assume $\rho_o = 11 \text{ Mg m}^{-3}$, $g_c = 10.7 \text{ m s}^{-2}$, $\beta = 1$, $\mu_o = 4\pi \times 10^{-7} \text{ H m}^{-1}$, $D = 2.258 \times 10^6 \text{ m}$, $R = r_i/r_c = 0.35$, and $\dot{\chi}_o - \dot{\chi}_{cr} = 3 \times 10^{-19} \text{ s}^{-1}$. Using these values along with $\gamma = 0.1$, (17) yields $B_d^{cmb} \simeq 0.21 \text{ mT}$, slightly less than the present-day rms geomagnetic dipole intensity on the CMB of approximately 0.26 mT and quite comparable to the time-average value as inferred from paleomagnetic intensity data (Tauxe and Yamazaki, 2007). In addition to consistent dipole scaling, these mostly compositionally driven dynamos have another important attribute that makes them particularly useful for modeling geodynamo reversal behavior: their transition from dipole-dominant to multipolar field configurations occurs at a larger Ra -value than the minimum Ra -value where polarity reversals first occur (Kutzner and Christensen, 2002). This means there exists a Rayleigh number interval in these dynamos where the dipole component dominates the time average external field structure, yet the dipole fluctuations are large enough for the field to occasionally reverse polarity. Our study is conducted within this limited range of Ra -values.

In this paper, we do not analyze the internal mechanisms for reversals and excursions in our dynamos, except to note that they follow the same basic sequence of events described in Olson et al. (2009). A variety of reversal mechanisms have already been identified in numerical dynamos (see GCHR99, KC04; Wicht and Olson, 2004; Wicht, 2005; WSH08; Aubert et al., 2008; Rotvig, 2009). It is likely that some of the differences in the reversal frequencies reported in these studies are attributable to the diverse ways in which reversals can initiate and develop. Consider for example the issue of where the reversed magnetic flux that initiates the polarity event first appears. GCHR99 and Wicht and Olson (2004) report the first appearance of reversed flux inside and outside the tangent cylinder, respectively. Rotvig (2009) finds that the first appearance of reversed flux depends on the mode of heating, and is different for internally versus basal heated dynamos. In order to minimize this type of ambiguity, only a limited range of dynamo parameters are considered in this study. Specifically, we analyze dynamos with outer boundary conditions that deviate by relatively small amounts from a baseline uniform boundary case, and are otherwise identical.

5. Results

Results of 17 dynamos with different patterns of boundary thermal forcing are summarized in Table 1. For each dynamo, Table 1 gives the boundary forcing planform, its average heat flux and the amplitude of its spatial variation, the model run time, the rms internal magnetic field (time average and standard deviation), the rms fluid velocity expressed as magnetic Reynolds number Rm (time average and standard deviation), the rms dipole magnetic field amplitude on the outer boundary (time average and standard deviation), the rms axial dipole magnetic field amplitude on the outer boundary (time average and standard deviation), all in dimensionless form, plus the number of reversals and excursions. For the axial dipole, polarity sensitivity is included in the time average. In order to facilitate comparisons, these dynamos all have the same values

Table 1
Summary of dynamo cases.

CMB	$\bar{f}_c \pm \delta f_c$	Time	B_{rms}^v	Rm	B_d	B_a	N_{rev}	N_{exc}
–Y40	0 ± 0.045	40	4.95 ± 0.56	156 ± 10	0.535 ± 0.160	0.525 ± 0.15	1	0
U	0 ± 0	267	4.03 ± 0.73	155 ± 13	0.534 ± 0.210	0.312 ± 0.441	6	4
Y22	0 ± 0.06	130	3.76 ± 1.12	158 ± 13	0.469 ± 0.283	0.382 ± 0.325	4	5
Y2211	0 ± 0.045	119	4.25 ± 0.84	155 ± 13	0.591 ± 0.307	0.057 ± 0.642	8	11
–Y20	0 ± 0.045	40	2.58 ± 0.71	170 ± 8	0.210 ± 0.125	-0.011 ± 0.24	3	2
Y11	0 ± 0.06	165	4.04 ± 0.87	155 ± 15	0.509 ± 0.234	0.088 ± 0.519	18	7
+Y40	0 ± 0.045	40	4.19 ± 0.78	153 ± 13	0.519 ± 0.242	-0.128 ± 0.50	5	4
+Y20	0 ± 0.045	40	3.73 ± 0.69	154 ± 14	0.337 ± 0.208	0.057 ± 0.64	19	16
Y10	0 ± 0.045	120	4.25 ± 0.83	156 ± 14	0.536 ± 0.307	0.080 ± 0.330	8	11
T–2	$-0.045 \pm .06$	265	3.68 ± 0.30	111 ± 12	0.674 ± 0.084	0.620 ± 0.073	0	0
T–1	$-0.023 \pm .06$	265	3.82 ± 0.85	134 ± 14	0.585 ± 0.217	0.039 ± 0.559	6	2
T0	0 ± 0.06	262	3.85 ± 1.02	157 ± 15	0.483 ± 0.258	0.002 ± 0.492	23	5
T+1	$+0.023 \pm .06$	61	4.05 ± 0.86	173 ± 17	0.390 ± 0.226	0.001 ± 0.413	12	20
T0+1	0 ± 0.08	40	3.93 ± 1.22	158 ± 16	0.520 ± 0.290	$-.394 \pm 0.321$	3	3
T0+2	0 ± 0.12	40	3.13 ± 1.56	166 ± 18	0.361 ± 0.272	0.071 ± 0.381	8	3
T0+3	0 ± 0.16	40	2.64 ± 1.43	172 ± 19	0.230 ± 0.215	0.066 ± 0.239	8	6
T0+4	0 ± 0.24	25	2.77 ± 0.99	176 ± 19	0.211 ± 0.202	-0.045 ± 0.225	10	8

CMB = Outer boundary conditions: U = uniform; Y = harmonic, [+ , –] prefixes = equatorial heat flux anomaly; T = tomographic (T0 = adiabatic; T+1 = superadiabatic; T–1, etc. = subadiabatic cases; T0+1, etc. = larger amplitude heterogeneity); \bar{f}_c , δf_c = boundary heat flux parameters defined in text; time in dipole decay units; B_{rms}^v = volume averaged (rms) magnetic field; Rm = magnetic Reynolds number of rms velocity; B_d , B_a = rms dipole, axial dipole at r_c ; N_{rev} , N_{exc} = number of reversals, excursions. Means (time averages) with standard deviations for B and Rm .

of E , Pr , Pm and the chemical Rayleigh number Ra and differ only in the pattern and magnitude of their outer boundary heat flow. Table 1 includes a uniform boundary heat flow case labeled U, harmonic forcing cases labeled Y, and several cases with tomographic forcing labeled T.

The uniform U-case is purely chemical convection, with $\bar{f}_c = \delta f_c = 0$, which corresponds to exactly adiabatic heat flux at the CMB in the core. We use this case as a baseline for comparison with the heterogeneously forced dynamos. Although an adiabatic heat flux at the CMB eliminates thermal boundary layer instabilities below the CMB that may be important in the core (see GCHR99), it makes a good reference case because small deviations from adiabatic heat flow on the outer boundary can produce relatively large changes in the reversal frequency. The harmonic Y-cases also have zero average boundary heat flux $\bar{f}_c = 0$ and have boundary heat flux variations proportional to a single harmonic (denoted by Y11, for $\ell = m = 1$, etc.) or in one case the sum of harmonics Y22 and Y11, denoted by Y2211. Plus (+) and minus (–) prefixes to the zonal cases Y20 and Y40 denote the sign of their equatorial heat flow anomaly. Note that this convention differs from KC04, who used the sign of the normalized spherical harmonic as the prefix.

For the Y-cases, the dimensionless amplitudes of boundary heat flux heterogeneity δf_c are nearly the same (though not identical) so these mainly offer planform comparisons. The differences between the various T-cases involve the magnitude of the average boundary heat flux and the amplitude of their heterogeneity, so these offer amplitude comparisons. Case T0 has $\bar{f}_c = 0$ whereas cases T–2, T–1, and T+1 have $\bar{f}_c = -2h$, $-h$, and $+h$ respectively, where $h = 0.0225$ is the dimensionless unit of the average outer boundary heat flow. According to this definition, negative values of h in our models correspond to subadiabatic heat flux at the CMB, and positive h -values correspond to superadiabatic heat flux at the CMB. All of these T-cases have the same heterogeneity amplitude $\delta f_c = 0.06$. The cases labeled T0+1 . . . T0+4 in Table 1 are otherwise similar to case T0 except that the amplitude of their boundary heterogeneity is progressively larger.

5.1. Effects of boundary heat flux pattern on reversal rate

Fig. 1 shows the average frequency of polarity reversals and total polarity events (reversals plus excursions) per dipole decay time for the 17 dynamos in Table 1, organized in three groups. The first group consists of the baseline U-case and the Y-cases,

all of which have zero average heat flux on the outer boundary. The second group consists of the T-cases with increasing average boundary heat flux but equal boundary heat flux heterogeneity. The third group consists of T-cases with zero average boundary heat flux but increasing boundary heat flux heterogeneity. The sequencing in Fig. 1 is also in order of increasing average equatorial heat flux on the outer boundary, from left to right within each group (the sequencing of cases with the same average equatorial heat flux is according to reversal frequency). The dashed lines are the mean polarity event rates for all the dynamos excepting the two

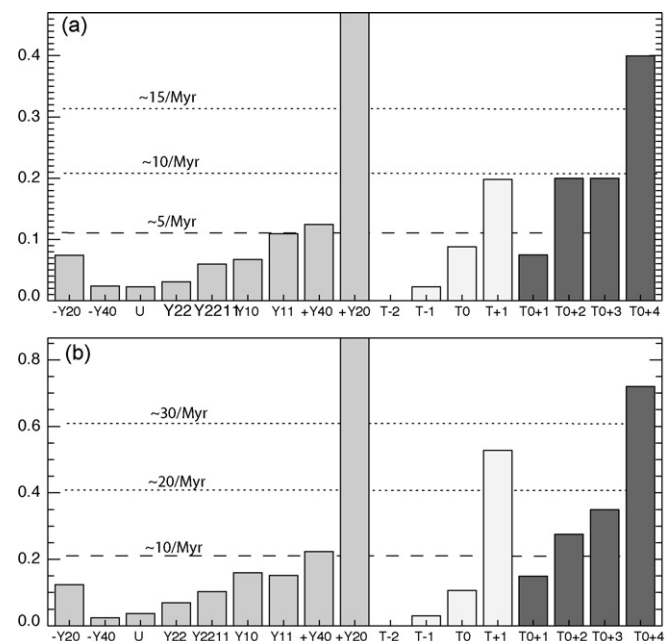


Fig. 1. Average frequencies of polarity events per dipole decay time for dynamos with various types of outer boundary heat flux heterogeneity. Polarity reversals (a) and reversals plus excursions (b). (U,Y,T) denote uniform, harmonic, and tomographic boundary heat flux patterns, respectively, as defined in Table 1. The first group have variable heat flux heterogeneity patterns, the second group have variable average heat flux, the third group have variable amplitude of heat flux heterogeneity. Dashed lines are average event rates excluding cases +Y20 and T–2; dotted lines show one and two standard deviations. Approximate paleomagnetic frequencies shown as events per Myr assumes 20 kyr for the geomagnetic dipole free decay time.

extreme cases + Y20 and T–2, and the dotted lines indicate one and two standard deviations, respectively, above the means. The corresponding paleomagnetic frequencies are shown in units of polarity events per million years, assuming 20 kyr for the geomagnetic dipole free decay time.

Comparison of the baseline U-case, the Y-cases, and the T-cases with $\bar{f}_c = 0$, supports the interpretation that outer boundary heat flux heterogeneity tends to increase reversal and excursion frequency, relative to uniform conditions. This is qualitatively similar to the results of GCHR99, who found that uniform boundary forcing is more stable to reversals than heterogeneous boundary forcing in most cases. The exception to this rule in Fig. 1 is the – Y40 case, which has the same reversal rate but a slightly lower total polarity event rate than the baseline U-case. The difference in polarity event rates between these two cases is very small compared to the standard deviation of all the cases, and is therefore not of great significance in our study. However, the results in Fig. 1 do not exclude the possibility of boundary heat flux patterns that are stabilizing. Previously, GCHR99 found two zonal patterns that were stabilizing (cases D and E, respectively, in their notation) corresponding to – Y20 and + Y40 in our notation. KC04 found that both – Y20 and – Y40 (in our notation) were stabilizing, but in contrast to GCHR99, KC04 found that + Y40 was destabilizing. Table 2 shows a qualitative comparison of results for these two zonal Y-cases from KC04, the present study, and GCHR99 as summarized by Coe and Glatzmaier (2006). There is full qualitative agreement for – Y20 and + Y20, but differences between GCHR99 and the other two studies for + Y40 and – Y40 (cases E and F, respectively, in the GCHR99 notation).

One of our motivations for comparing different harmonic patterns is to determine if the relative frequency of reversals can be predicted on the basis of simple symmetry considerations of the boundary thermal forcing. The results of the present study and KC04 can be rationalized by the inference that forcing less heat out of the equatorial region is a stabilizing mechanism, and conversely, forcing more heat out of the equatorial region is destabilizing. In contrast, the GCHR99 results are better rationalized by the inference that forcing more heat out of the polar regions is a stabilizing mechanism. The differences between these two interpretations may reflect internal model differences among the three studies, such as the relative importance of thermal versus compositional buoyancy, the vigor of convection inside versus outside the inner-core tangent cylinder, and the amount of superadiabatic CMB heat flux, for which GCHR99 use $\bar{f}_c \simeq 0.07$. GCHR99 suggest that their case + Y40 is stable and non-reversing because of the natural tendency for rapidly rotating convection to have a strong convective heat flux in the equatorial and polar regions compared to mid-latitudes, which conforms to the planform of heat flux at the outer boundary. They argue that, in the equatorial region, Coriolis, buoyancy, pressure gradient, and Lorentz forces all act primarily within planes parallel to the equator and therefore can remain in balance and so minimize destabilizing accelerations. Convective heat flux in the polar region is relatively large because Coriolis and Lorentz forces have little effect on radial velocities there. Flows at

mid-latitude cannot satisfy either condition and therefore tend to be weaker and more time dependent, so minimizing them via the boundary heat flux condition helps to stabilize the dynamo. Overall, however, Fig. 1 indicates that polarity event frequency is more sensitive to the amplitude of the average boundary heat flux or the amplitude of its heterogeneity, rather than the pattern of its heterogeneity.

Figs. 2 and 3 show the pattern of boundary thermal forcing for U-case and Y-case dynamos, scatter plots of the geomagnetic dipoles, and histograms (probability density functions, pdfs) of the geomagnetic dipole tilt angle, geomagnetic dipole longitude, and axial dipole amplitude. The relative frequency of reversals and excursions seen in Fig. 1 is mirrored in the statistical behavior of the various dynamos shown in Figs. 2 and 3. In particular, the more stable (less frequently reversing) U-case has a generally stronger axial dipole field and less dispersion in dipole axis locations compared to the more frequently reversing heterogeneous boundary cases, which agrees with the GCHR99 results (Coe and Glatzmaier, 2006). For example, compare the U-case in Fig. 2 with the frequently reversing Y-cases in Fig. 3. The axial dipole pdf of the U-case is strongly bimodal, with only slight overlap of the reverse and normal polarity modes near zero, indicating this dynamo spends little time in the weak dipole, multipolar transition state. In contrast, the axisymmetric cases Y10 and + Y20 in Fig. 3 have strong modes centered around zero axial dipole, indicating these dynamos spend considerable time in the weak dipole, multipolar state. Indeed the axial dipole pdfs of the $\pm Y20$ -cases are basically unimodal in this regard, in that they lack significant peaks corresponding to the stable axial dipole polarities. Several of the dynamos in Figs. 2 and 3 show persistent (long-lasting) polarity biases, including the U-case, in spite of it being run for hundreds of dipole decay times. The magnitude of the polarity bias for each case is indicated by the ratio of mean to the standard deviation of the axial dipole B_a in Table 1, with large values of this ratio corresponding to large polarity bias. Persistent polarity bias in numerical dynamos has been noted previously, including in models run for more than 100 Myr that reversed dozens of times (see WSH08 for an example). We note that the paleomagnetic reversal record shows little evidence of long-lasting polarity bias apart from superchrons (Merrill et al., 1996), and the causes of long-lasting polarity bias in reversing dynamo models remain unclear.

Systematic longitude bias of the geomagnetic pole is clearly evident in the non-axisymmetric Y-cases in Fig. 2, and some residual scatter is evident in the geomagnetic pole longitudes of some of the axisymmetric Y-cases in Fig. 3. The systematic longitude bias in the non-axisymmetric Y22- and Y2211-cases correspond to the longitudes of the boundary heat flux maxima. Similar concentrations of radial magnetic field have been seen in many previous dynamo simulations with heterogeneous thermal forcing (GCHR99; Coe et al., 2000; KC04; Willis et al., 2007; Aubert et al., 2008). The standard explanation for these field concentrations is that the core fluid is anomalously cool beneath regions of high boundary heat flux, and therefore fluid downwellings preferentially form at these spots. As demonstrated in KC04, these downwellings induce horizontal convergence, which locally concentrate the radial magnetic field. The Y11-case also shows two geomagnetic pole concentration maxima. These occur near longitudes 140 and 320, respectively, 180° apart but shifted by nearly 40° from the heat flux maxima. The longitude shift is due in this case to a residual, large scale azimuthal order $m = 1$ circulation driven by the boundary heterogeneity. Also in this case, the apparent confinement of the magnetic polarity by the boundary heterogeneity at two preferred longitudes rather than one is an artifact of polarity. The dipole axis is actually confined to a single longitude band, and the two apparently preferred longitudes correspond to pole locations for the reverse and normal polarity states, respectively.

Table 2

Axisymmetric outer boundary (CMB) heat flux heterogeneity patterns and their polarity reversal frequencies relative to uniform boundary heat flux, according to CG06 Coe and Glatzmaier, 2006, KC04 Kutzner and Christensen, 2004 and this study.

Heat flux pattern	Relative reversal frequency					
	CMB	POLE	EQ	CG06	KC04	This study
–Y20	max	min	min	Lower	Lower	Lower
+Y20	min	max	max	Higher	Higher	Higher
+Y40	max	max	max	Lower	Higher	Higher
–Y40	min	min	min	Higher	Lower	Lower

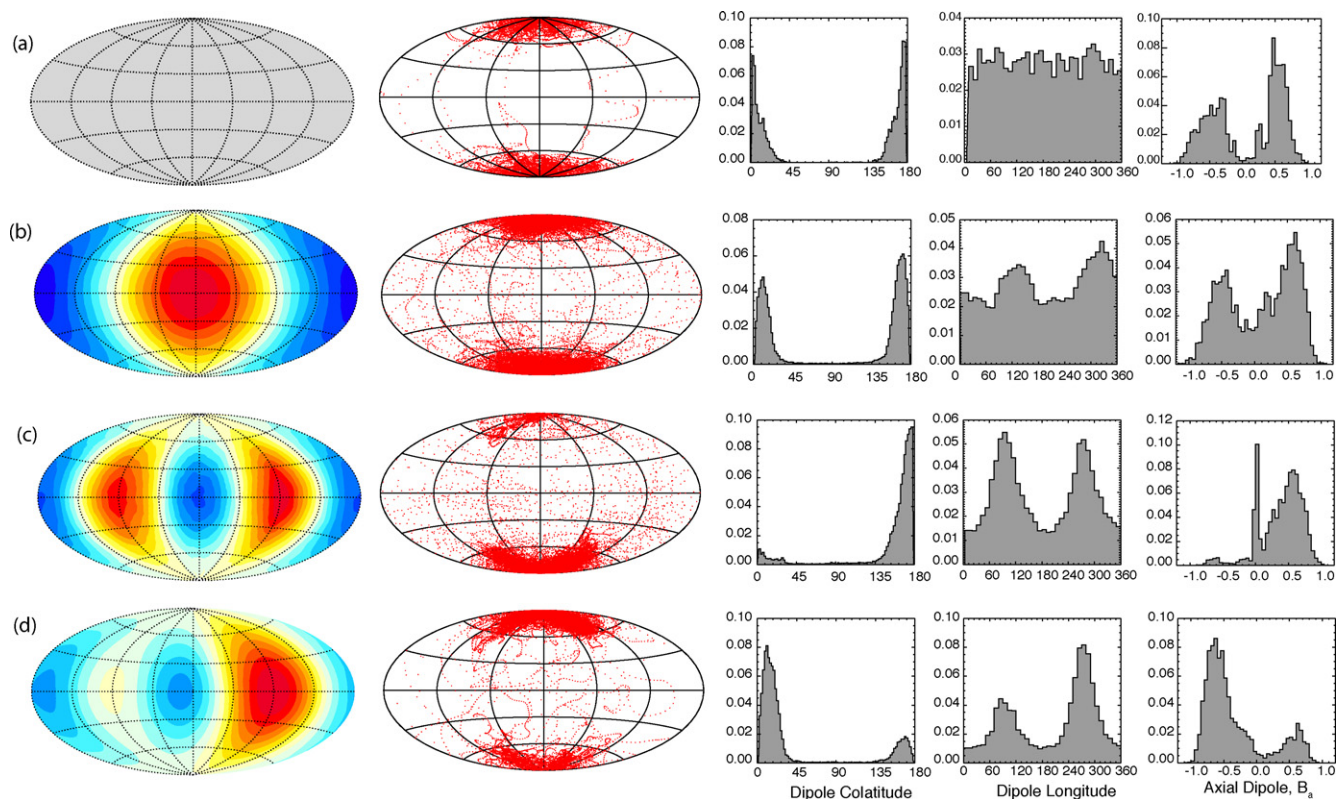


Fig. 2. Summary of results from dynamos with harmonic boundary forcing (Y-cases) and the dynamo with uniform boundary forcing (U-case) as defined in Table 1. Rows from top to bottom: case U (a), Y11 (b), Y22 (c) and Y2211 (d). Columns from left to right: boundary heat flux contours (red = positive; blue = negative); scatter of dipole axis locations; dipole co-latitude histogram; dipole longitude histogram; axial dipole intensity histogram. Aitoff projections for maps (For interpretation of the references to color in this figure legend, the reader is referred to the web version of the article).

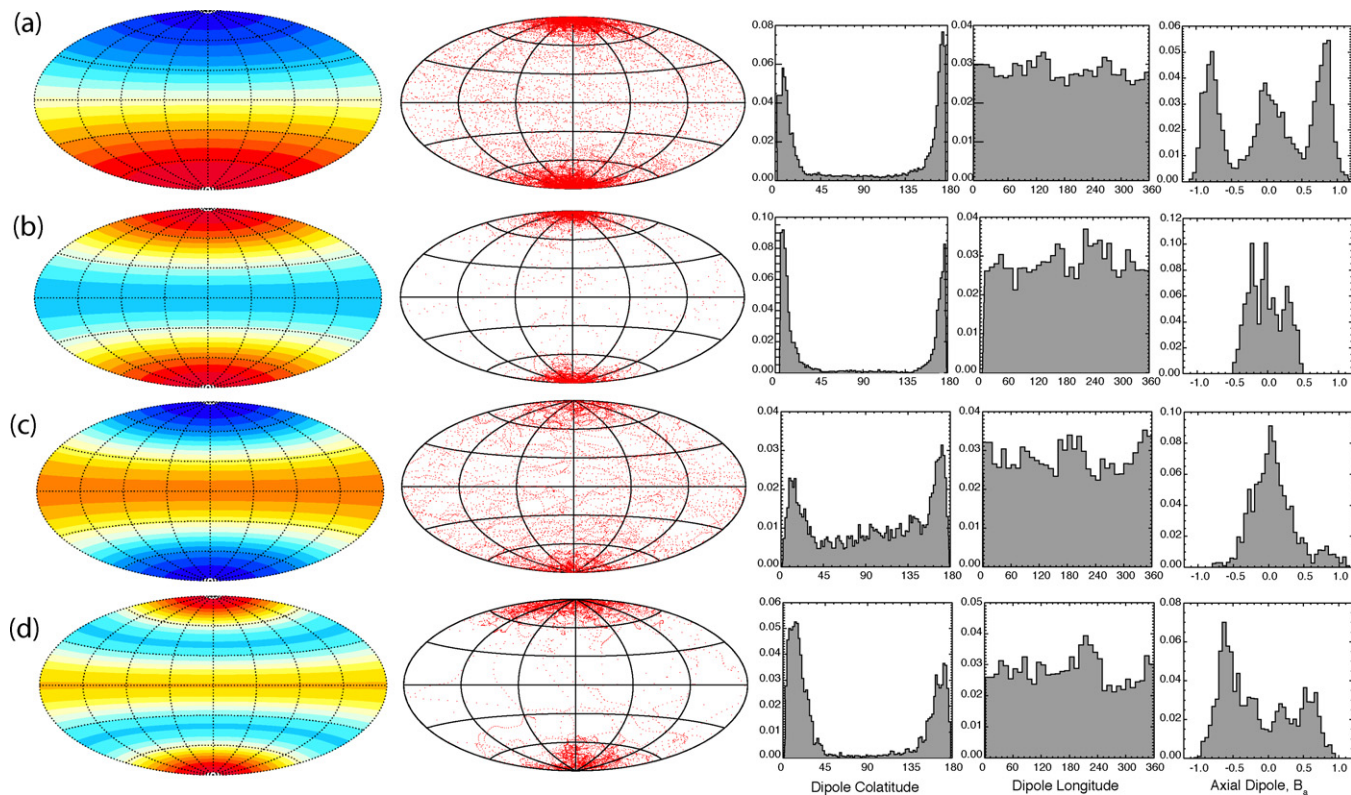


Fig. 3. Summary of additional results from dynamos with harmonic boundary forcing (Y-cases) as defined in Table 1. Rows from top to bottom: case Y10 (a), $-Y20$ (b), $+Y20$ (c) and $+Y40$ (d). Columns from left to right: boundary heat flux contours (red=positive; blue=negative); scatter of dipole axis locations; dipole co-latitude histogram; dipole longitude histogram; axial dipole intensity histogram. Aitoff projections for maps.

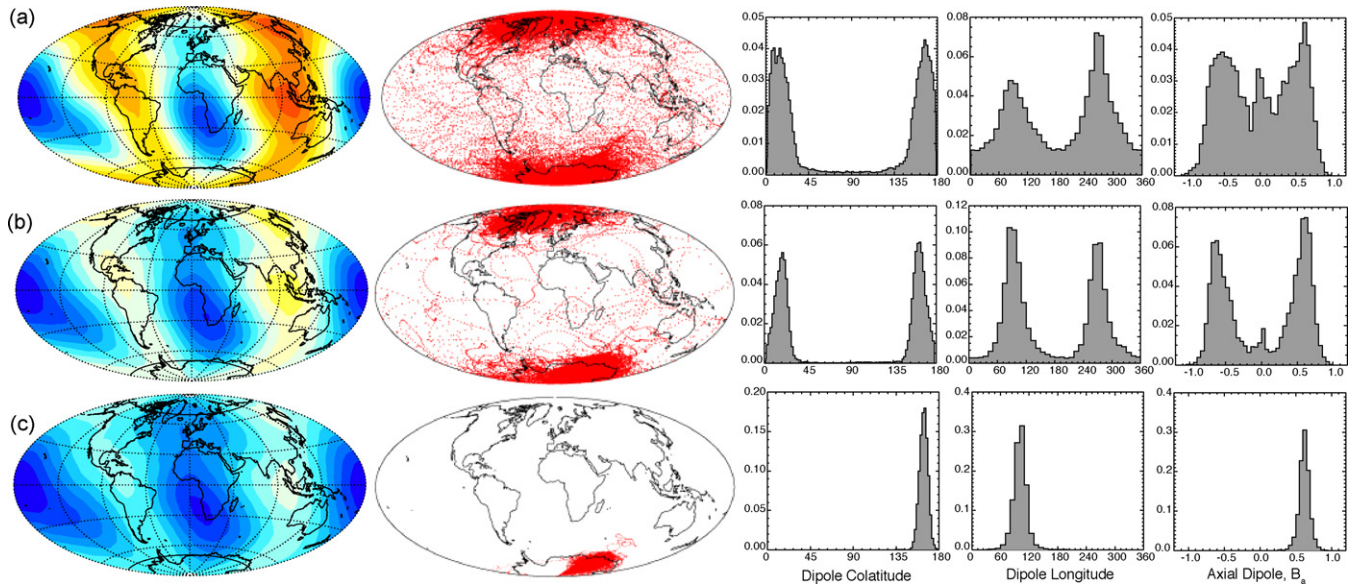


Fig. 4. Summary of results from three dynamo with tomographic boundary forcing (T-cases) as defined in Table 1. Rows from top to bottom: case T0 (a), T–1 (b) and T–2 (c). Columns from left to right: boundary heat flux contours (red = positive; blue = negative); scatter of dipole axis locations; dipole co-latitude histogram; dipole longitude histogram; axial dipole intensity histogram. Aitoff projections for maps, with continental outlines shown for reference (For interpretation of the references to color in this figure legend, the reader is referred to the web version of the article.).

5.2. Tomographic dynamo results

The sequencing of the T-cases in Fig. 1 shows that reversal and excursion frequency increase systematically with the total outer boundary heat flow and also with the amplitude of the heat flux heterogeneity. Cases T–2 and T–1 have negative total heat flow at the outer boundary (corresponding to subadiabatic boundary heat flow in the compressible outer core), cases T0 and T0+1...T0+4 have zero total boundary heat flow, with case T0+4 having four times the amplitude of boundary heat flux heterogeneity compared to case T0. Only case T+1 has a positive total boundary heat flow (corresponding to superadiabatic boundary heat flow in the outer core). The non-dimensional amplitude of the mean boundary heat flux for cases T–2, T–1, T0 and T+1 are given in Table 1, and the boundary heat flux patterns corresponding to these cases are shown in Fig. 4.

No reversals or excursions were recorded in case T–2. Inspection of the time series of dipole field intensity and dipole tilt angle in Fig. 5 for this case shows that, except for one brief and relatively minor tilt event, dynamo T–2 never deviated appreciably from a stable dipole-dominated configuration with its dipole axis slightly inclined to the rotation axis, over the equivalent of 5.2 Myr of paleomagnetic time. The distribution of dipole axis locations and dipole longitudes in Fig. 4 show strong concentration beneath the Eastern hemisphere portion of Antarctica, with (80S, 108E) being the most frequent geomagnetic pole location, and corresponding to the longitude of the largest positive boundary heat flow heterogeneity. Similarly, the distribution of axial dipole intensities in Fig. 4 are tightly concentrated around a value 0.62 in this case. Case T–2 has the characteristics of a globally locked dynamo (Sumita and Olson, 2002; Willis et al., 2007), the locking provided by the strong influence of the boundary heat flow heterogeneity. In this particular case the dynamo is also non-reversing, by virtue of the stabilizing effects of the subadiabatic total boundary heat flow.

Increasing the total boundary heat flow in the tomographic dynamo systematically increases their level of time variability and increases their frequency of reversals and excursions. The systematic increase in T-case reversal and excursion frequencies with total heat flow seen in Fig. 1 is also reflected in the increased scatter of pole locations and dipole intensities shown in Fig. 4. Case T–1 has

exactly one-half of the (negative) total boundary heat flow of case T–2, and it also displays global locking, in that the dipole axis locations cluster tightly about a preferred location, near (77S, 90E) in this case. There is a complementary cluster of pole locations near (77N, 90W) which represents the reversed pole locations. Although this dynamo is essentially locked with respect to pole longitude, it nevertheless reverses polarity on occasion, and despite reversing, its time average state includes an inclined dipole axis.

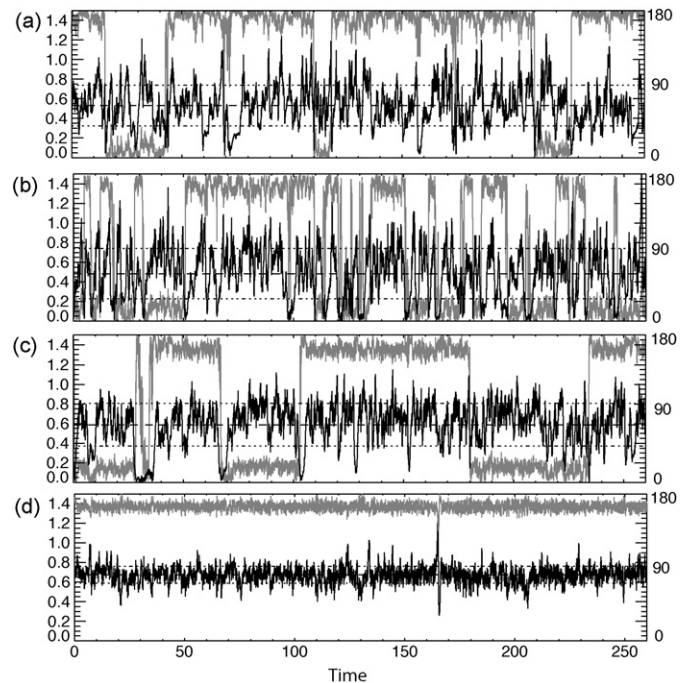


Fig. 5. Time series of dimensionless rms dipole strength (black; left scale) and dipole co-latitude in degrees (grey; right scale) from three dynamo with tomographic boundary forcing (T-cases) and the dynamo with uniform boundary forcing (U-case) as defined in Table 1. Rows from top to bottom: case U (a), T0 (b), T–1 (c) and T–2 (d). Dashed line is time average dipole strength and dotted lines denote one standard deviation. Time is in dipole decay units.

Cases T0, T0+1... T0+4 differ only in the amplitude of their boundary heat flux heterogeneity. Like the previous group of T-cases, the polarity event frequencies increase monotonically with boundary heterogeneity amplitude, although the reversal frequency in cases T0+2 and T0+3 are the same. Overall, the sensitivity of reversal frequency to boundary heat flux heterogeneity amplitude is not as great as was found for the mean boundary heat flux. In addition, Table 1 shows that the cases in this group with the highest polarity event frequency also have rather weak dipole field amplitudes B_d , which may account for their lack of stability.

Case T0 is perhaps our most nominally Earth-like T-case in terms of its reversal frequency. It exhibits local-style locking behavior (Sumita and Olson, 2002) because it produces two bands of preferred pole longitudes for each polarity, corresponding to the two longitude bands with higher than average boundary heat flow. In addition, its axial dipole pdf is trimodal, with two primary modes corresponding to the stable, strong dipole field polarities, and a smaller mode corresponding to the weak dipole transition field configuration. In terms of overall behavior, the T0 cases behave like cases Y22 and Y2211, as would be expected on the basis of the strong degree $\ell=2$ and significant $\ell=1$ signatures in the lower mantle seismic tomography model. Lastly, cases T+1, T0+3, and T0+4 are essentially multipolar dynamos with behavior similar to cases \pm Y20 shown in Fig. 3. In these cases the heightened magnetic field variability is probably due to the enhanced convection from the elevated outer boundary heat flow (note their large magnetic Reynolds numbers in Table 1); this variability destabilizes the axial dipole and prevents long stable polarity epochs.

Fig. 5 compares time series of rms dipole field intensity on the outer boundary and dipole axis tilt from the uniform boundary heat flow case with tomographic heat flow cases T0, T-1 and T-2 over 260 dipole decay times, equivalent to approximately 5.2 Myr of paleomagnetic time. The dashed and dotted lines indicate the mean (time average) dipole intensity and its standard deviation, respectively. The overall level of magnetic field variability is comparable in the three reversing T-cases, and significantly less only in the non-reversing case T-2. The main systematic difference between the cases in Fig. 5 is an inverse relationship between the mean (time average) dipole intensity and the reversal frequency. Note that the frequency of reversals in the uniform boundary U-case is intermediate between case T0 with zero total boundary heat flow and case T-1 with a slightly negative (i.e., subadiabatic) total boundary heat flow. This is another demonstration that boundary heat flow heterogeneity tends to promote dynamo reversals, compared to uniform boundary conditions.

5.3. Dynamo symmetries, flow velocity, and reversal frequency

A variety of global dynamo properties have been proposed as diagnostics for the frequency of polarity reversals, including the equatorial symmetry of the magnetic field on the CMB (Coe and Glatzmaier, 2006), the local Rossby number of the core flow (Christensen and Aubert, 2006; WSH08), and the equatorial symmetry of the core flow (Olson et al., 2009). Geomagnetic field symmetry on the CMB is usually represented by splitting the Lowes energy spectrum of the field into its equatorially anti-symmetric and equatorially symmetric parts (Roberts, 1971). The anti-symmetric part of the poloidal magnetic field is called the odd or dipole family, because a geocentric axial dipole field has this particular symmetry, and for similar reasons the symmetric part of the Lowes spectrum is called the even or quadrupole family. Here we denote these two families by o and e , respectively. The components of the fluid velocity and magnetic field inside the dynamo include both poloidal and toroidal parts, which can be decomposed into their equatorially symmetric and anti-symmetric parts, here denoted by s and a , respectively. For the fluid velocity, we use the

tangential velocity components at $0.9r_c$ to compute the symmetric and anti-symmetric parts of the spherically averaged kinetic energy KE . For the internal magnetic field, we use all three components to compute the volume averaged magnetic energy ME . For the external magnetic field we use the radial component on the outer boundary B_r . A related statistic is the dipolarity d , the ratio of the rms dipole intensity B_d to the rms total field intensity B_{rms} on the outer boundary. In Table 3 we give for each model the time average and the standard deviation of the following ratios: $KE(s/s+a)$, $ME(a/s+a)$, $B_r^2(o/e+a)$, $B_r^2(o/e)$, along with the dipolarity and the local Rossby number Ro_l , defined as

$$Ro_l = \frac{\ell}{\pi} ERmPm^{-1} \quad (18)$$

where ℓ is a characteristic harmonic degree of the flow, obtained from the kinetic energy spectrum (see Christensen and Aubert, 2006).

Fig. 6a–d shows correlations between polarity event frequency (reversals plus excursions) and the ratios $KE(s/s+a)$, $B_r^2(o/e)$, the local Rossby number Ro_l , and the dipolarity d , respectively. Larger values of the ratio $B_r^2(o/e)$ show little direct correlation with polarity event frequency, but for smaller values of this ratio there appears to be a threshold around $B_r^2(o/e) \simeq 1.2$, below which the polarity event frequency suddenly becomes large, irrespective of dynamo type. Another interesting property of this correlation is that none of our dynamos have $B_r^2(o/e)$ ratios below 0.8. It is perhaps significant that all but one of the frequently reversing cases in our study fall within this narrow range of $B_r^2(o/e)$ -ratio, irrespective of whether they are of the dipole-dominant or multipolar type. However, the clustering also means that dynamos within this narrow range have widely different reversal frequencies, which limits the predictive value of this diagnostic.

In contrast, the other diagnostics in Fig. 6 seem to depend more strongly on the dynamo type. $KE(s/s+a)$ -ratio generally decreases with increasing polarity event frequency, although there is more scatter in this diagnostic, particularly among the Y-cases in Fig. 6. The dipolarity and local Rossby number correlations are approximate mirror images of each other, with event frequency generally increasing with Ro_l and generally decreasing with d . However, discernible trends are evident only within similar groups of the T-dynamos. Although the adiabatic T-cases with variable heterogeneity amplitude and the non-adiabatic T-cases with fixed heterogeneity amplitude follow qualitatively similar trends, their sensitivity to Ro_l and d are not identical. More significantly, the Y-cases do not show same trend as either group of the T-cases, particularly in terms of Ro_l .

Fig. 7 is a regime diagram showing reversal behavior and relative dipole field dominance versus dipolarity d and local Rossby number Ro_l . For reference, the dipolarity of the present-day geomagnetic field on the CMB is 0.48–0.63, the upper limit corresponding to spherical harmonic degree $\ell = 12$ truncation of the core field, the lower limit corresponding to an extrapolation of the core field spectrum (Stacey and Davis, 2008), and the local Rossby number of the core has been estimated at 0.09 on the basis of dynamo model scaling (Olson and Christensen, 2006).

Following WSH08, we divide Fig. 7 into three regimes, labeled DN (dipolar non-reversing), DR (dipolar reversing), and MR (multipolar reversing), respectively. The dipolar and multipolar designations are based on the existence or absence of side lobes in their respective axial dipole histograms. The dashed lines indicate schematic (i.e., very approximate) boundaries between the three regimes. The overall character of the regimes in Fig. 7 is similar to WSH08, although the numerical values differ somewhat. For example, WSH08 find the DR regime (which they characterize as most Earth-like) for $0.07 < Ro_l < 1.1$ and $0.3 < d < 0.65$, whereas we find these types of dynamos for $0.05 < Ro_l < 0.07$

Table 3

Means (time averages) and standard deviations of each ratio, except * denotes ratio of the means.

CMB	KE ($s/s+a$)	ME ($a/s+a$)	$B_r^2(o/o+e)$	$B_r^2(o/e)^*$	d	Ro_l
–Y20	0.97 ± 0.02	0.76 ± 0.16	0.74 ± 0.17	3.88 ± 5.12	0.38 ± 0.13	0.07
–Y40	0.93 ± 0.04	0.74 ± 0.11	0.72 ± 0.15	1.96 ± 1.02	0.53 ± 0.10	0.06
U	0.90 ± 0.09	0.63 ± 0.15	0.65 ± 0.16	1.41 ± 0.89	0.45 ± 0.12	0.06
Y22	0.86 ± 0.13	0.67 ± 0.16	0.67 ± 0.20	1.23 ± 0.98	0.40 ± 0.17	0.06
Y2211	0.77 ± 0.12	0.58 ± 0.05	0.57 ± 0.07	1.27 ± 1.01	0.47 ± 0.09	0.06
Y10	0.66 ± 0.17	0.56 ± 0.08	0.58 ± 0.11	1.44 ± 1.14	0.47 ± 0.13	0.06
Y11	0.78 ± 0.15	0.59 ± 0.10	0.62 ± 0.11	1.48 ± 1.26	0.45 ± 0.10	0.06
+Y40	0.80 ± 0.13	0.57 ± 0.08	0.54 ± 0.05	1.10 ± 0.96	0.44 ± 0.08	0.06
+Y20	0.55 ± 0.10	0.50 ± 0.04	0.51 ± 0.06	1.07 ± 1.32	0.35 ± 0.10	0.06
T–2	0.84 ± 0.07	0.62 ± 0.05	0.56 ± 0.05	1.25 ± 1.16	0.55 ± 0.04	0.04
T–1	0.81 ± 0.12	0.59 ± 0.09	0.55 ± 0.10	1.06 ± 0.76	0.48 ± 0.09	0.05
T0	0.79 ± 0.13	0.55 ± 0.09	0.55 ± 0.10	1.09 ± 0.80	0.42 ± 0.11	0.06
T+1	0.51 ± 0.13	0.50 ± 0.05	0.53 ± 0.08	1.15 ± 1.15	0.37 ± 0.11	0.07
T0+1	0.79 ± 0.06	0.52 ± 0.03	0.47 ± 0.04	0.85 ± 0.78	0.43 ± 0.10	0.06
T0+2	0.76 ± 0.18	0.54 ± 0.05	0.45 ± 0.09	0.80 ± 0.64	0.35 ± 0.11	0.07
T0+3	0.64 ± 0.20	0.51 ± 0.01	0.51 ± 0.08	0.95 ± 0.75	0.29 ± 0.10	0.07
T0+4	0.65 ± 0.12	0.51 ± 0.01	0.51 ± 0.06	0.85 ± 0.83	0.24 ± 0.10	0.07

KE is spherically averaged kinetic energy ratio, ME is the volume averaged magnetic energy ratio, B_r is radial magnetic field at $r = r_c$. s, a, o, e , denote equatorially symmetric, anti-symmetric, odd, and even parts, respectively. d is the dipolarity and Ro_l is the local Rossby number as defined in the text.

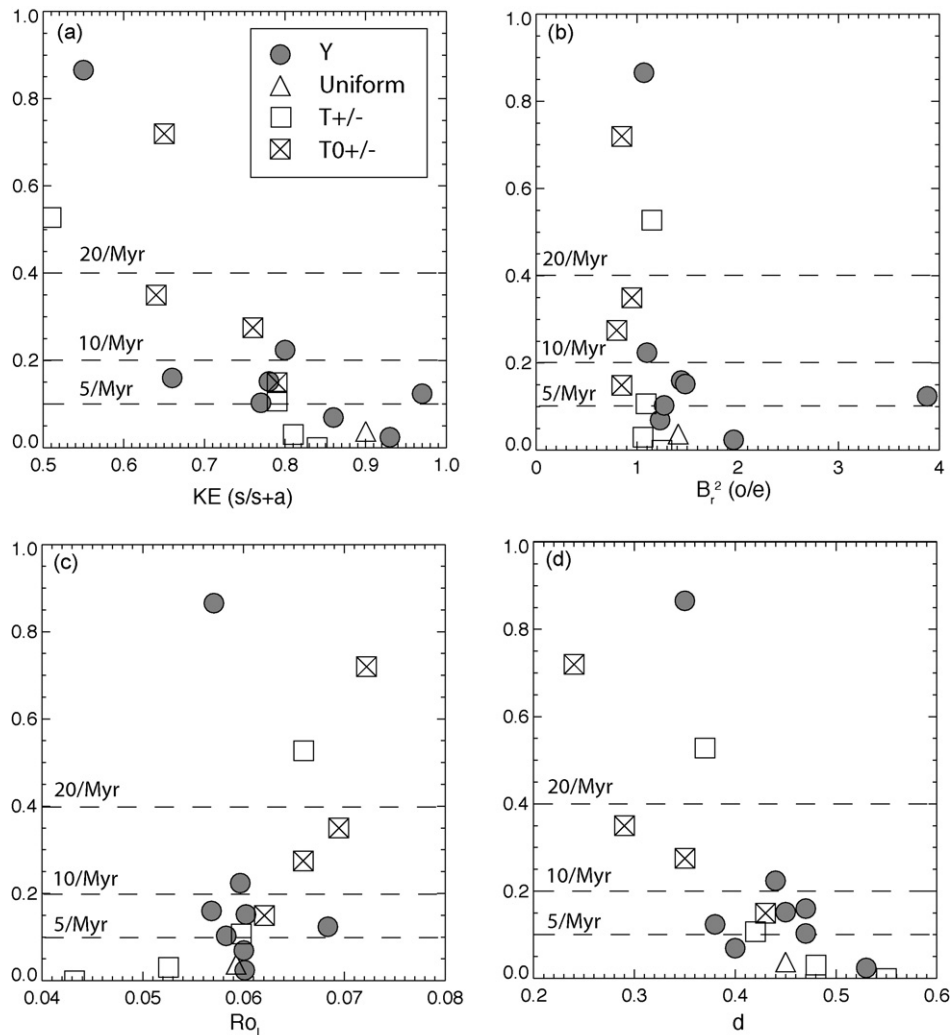


Fig. 6. Correlations of average event frequency (reversals plus excursions) per dipole decay time with four diagnostics given in Table 3 and defined in the text. Upper row: (a) Kinetic energy symmetry at radius $0.9r_c$; (b) magnetic field symmetry at outer boundary r_c ; lower row: (c) local Rossby number of the flow; (d) time average dipolarity. Symbols in the inset box indicate the dynamo case type. Labeled dashed lines indicate corresponding paleomagnetic frequencies, assuming 20 kyr for the geomagnetic dipole free decay time.

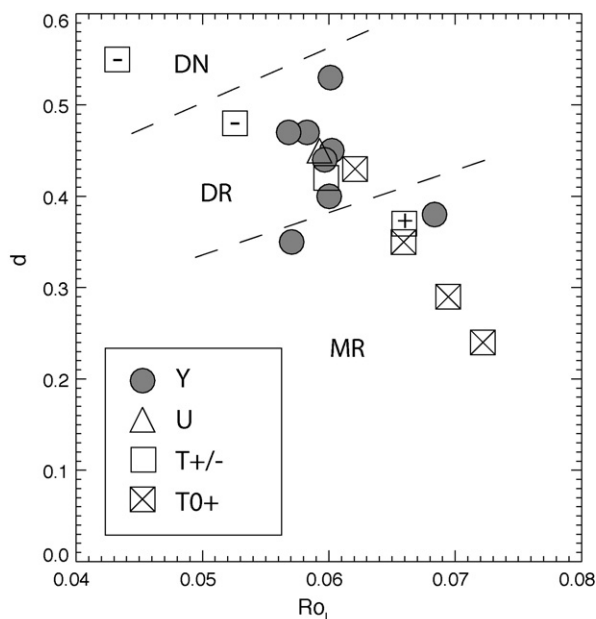


Fig. 7. Regime diagram of dipole field and reversal behavior as a function of dipolarity d and local Rossby number Ro_l for all dynamos. Symbols in the inset box indicate the dynamo case type. DN = Dipolar non-reversing, DR = dipolar reversing, MR = multipolar reversing regimes, respectively. The dashed lines are schematic regime boundaries.

and $0.37 < d < 0.53$. Some of these differences may be due to sparse coverage in Fig. 7, but some may be due to differences in the dynamo models themselves. In particular, the regime diagram in WSH08 is mostly based on dynamos with constant co-density outer boundary conditions, whereas we use only dynamos with co-density flux conditions on the outer boundary. It has been shown that these two boundary conditions can produce substantially different dipole field strengths in some numerical dynamos (Sakuraba and Roberts, 2009). The DR regime, nominally the most Earth-like in Fig. 7, includes dynamos with all three types of boundary conditions, and several cases in this regime cluster around $Ro_l = 0.06$ and $d = 0.45$. There is an overall increase in polarity event frequency from upper left to lower right in this regime. Note also that the most frequently reversing Y-cases, the superadiabatic T-cases, and the large-amplitude heterogeneity T-cases are characterized by low d -values (weak dipole fields) and fall within the MR regime.

6. Discussion and implications

We find that heterogeneity in outer boundary heat flux tends to increase the frequency of polarity reversals and excursions in our numerical dynamos, compared to otherwise similar dynamos with uniform boundary heat flux, generally consistent with the findings of GCHR99 and KC04. More importantly, we find that the total boundary heat flow (average boundary heat flux) has a strong influence on reversal and excursion frequencies, as evidenced in our dynamos with tomographic forcing. Increasing the total boundary heat flow increases the frequency of reversals and excursions, whereas reducing the total boundary heat flow reduces their frequency. Our tomographic models also show a positive correlation between the amplitude of the boundary heat flux heterogeneity and the polarity event frequency, although boundary heterogeneity also tends to weaken the dipole field.

The sensitivity of reversal frequency to boundary heat flow pattern is more complex. Our dynamos with zonal harmonic thermal forcing consisting of one axisymmetric spherical harmonic show increased reversal frequency in cases where the equatorial bound-

ary heat flux is high, and reduced reversal frequency in cases where the equatorial heat flux is low. In contrast to this sensitivity to equatorial heat flux, we do not find clear sensitivity to the boundary heat flux in the polar regions, or to non-axisymmetric planform. Non-axisymmetric boundary heat flux heterogeneity acts to stabilize the longitude of the dipole axis. The dipole axis tends to dwell, or in some cases tends to lock, within longitude bands that coincide with anomalously high boundary heat flux. These behaviors are due to the formation of high intensity magnetic flux patches by downwellings at these longitudes, and leads to an overall longitude correlation between the field intensity and the heat flux on the boundary.

Applied to the core, our results indicate that increases (decreases) in the average equatorial heat flux, the total heat flow on the CMB, or the amplitude of its lateral heterogeneity, can increase (decrease) geomagnetic reversal frequencies. For example, non-reversing behavior is found in our tomographic model with the most subadiabatic average CMB heat flux. This does not imply that the core needs to be subadiabatic during geomagnetic superchrons, because non-reversing behavior is commonplace in dynamo models even with superadiabatic thermal stratification. Nevertheless, our results demonstrate that subadiabatic thermal conditions in the core tend to make geomagnetic reversals less frequent.

Our results have multiple implications for interpreting the paleomagnetic reversal record in terms of core–mantle thermal interaction. We find that relatively efficient ways to alter reversal frequency include changing the average equatorial heat flux or the total heat flow on the CMB. According to our models, reducing either parameter reduces the reversal frequency, with non-reversing states (possibly analogous to geomagnetic superchrons) corresponding to times with reduced total core heat flow compared to its long-term average level (Courtillot and Olson, 2007). A third, less efficient way to alter geomagnetic reversal frequency is to change the amplitude of the CMB heat flux heterogeneity. All of the above mechanisms imply changes in the intensity of convection in the core, with more frequent polarity events signifying more intense core convection. This particular relationship is implicit in the correlation between polarity event frequency and the local Rossby number in our models.

In terms of mantle dynamics, increasing the total core heat flow and the amplitude of its spatial heterogeneity implies more vigorous convection in the lower mantle. Planforms of lower mantle convection that have been proposed for the stages of supercontinent aggregation and breakup, for example, primarily involve non-axisymmetric harmonics such as Y11, Y22, and their combination (Zhong et al., 2007). These do not necessarily involve changes in equatorial or total CMB heat flow, or the amplitude of heat flux heterogeneity, so according to our results, they may not strongly affect geomagnetic reversal frequencies. Reconstructions of past locations of large igneous provinces suggest that the two prominent low seismic shear velocity structures in the deep mantle beneath Africa and the Pacific have not changed their near-equatorial locations much over the past 200 Ma (Burke et al., 2008), consistent with the interpretation that the non-axisymmetric part of the long wavelength planform of CMB heat flux has not changed very much over this time, although its amplitude may have varied.

According to our results, the fluctuations in total core heat flow that are required to transition the geodynamo from a reversing to a non-reversing state and back may be rather small. If the geodynamo fortuitously lies near the transition from reversing to non-reversing behavior, then on a percentage basis, the total superadiabatic CMB heat flow fluctuation needed to change its reversal frequency may be only about $\pm 20\%$ (Driscoll and Olson, 2009b), which could be one or even two orders of magnitude smaller than the total core heat flow, much of which is heat conducted down the core adiabat. A few percent change in CMB heat flow is comparable to the rela-

tive changes in other global geodynamic properties that are known to have varied over the past several hundred million years, such as continental magmatic activity (Ryan and Dewey, 1997), plate velocities and subduction rates (Cogne and Humler, 2004; Labrosse and Jaupart, 2006; Conrad and Lithgow-Bertelloni, 2006) and global sea level (Gaffin, 1987).

We comment on the difference between reversals and excursions as it affects our results. The distinction between geomagnetic reversals and excursions has a long and somewhat contentious history in the paleomagnetic literature (e.g., Cox and Dalrymple, 1967; Doell and Dalrymple, 1973; Harrison and Ramirez, 1975; Liddicoat and Coe, 1979; Hoffman, 1981; Coe et al., 1984; Merrill and McFadden, 1994; Langereis et al., 1997). Aside from the question of whether excursion records are real geomagnetic phenomena or rock-magnetic artifacts, most discussion has centered on whether excursions of the field direction are simply larger than normal secular variation or unsuccessful attempts to reverse. Further controversy stems from the multiple definitions of excursions that are used. In this paper we have used the conservative definition that the geomagnetic pole must depart by more than 90° from the rotation axis, a condition that Merrill and McFadden (1994), Langereis et al. (1997) termed 'reversal excursion.' Since then, however, precise dating of many excursions demonstrates that they define a global geomagnetic instability time scale (Singer et al., 2008). Moreover, detailed examination of the highest resolution excursion records in sediments shows that opposite polarity directions are reached more often than expected if only the non-dipole field were present, suggesting that some excursions should be regarded as aborted reversals (Valet et al., 2008). This view is also supported by dynamo model results. Glatzmaier and Coe (2007) illustrate an excursion from GCHR99 in which opposite polarity was reached briefly at most locations around the globe while flux of the original polarity remained deep in the core, mainly within the tangent cylinder. In the present study, Fig. 1 shows that the relative frequency of all polarity events (reversals and excursions lumped together) follows the same trends as for reversals alone.

One discrepancy between GCHR99 and our study concerns the effects of polar and equatorial heat flow on polarity reversals. Some of this discrepancy may be the result of different thermal boundary condition at the ICB. GCHR99 coupled the fluxes of independently computed heat and composition at the ICB to the local rates of cooling and inner core growth, whereas KC04 and the present study prescribe a volumetric sink of co-density. GCHR99 prescribed the total heat flux, both adiabatic and superadiabatic, at the CMB and consider positive average superadiabatic heat fluxes at the CMB, whereas only our T+1 case is superadiabatic. These differences in buoyancy production mechanisms may be partly responsible for the differences in how the models respond to the heterogeneous forcing. GCHR99 also has an inner core and mantle magnetically coupled to the fluid, both of which are free to rotate in response to the net torques acting on them. Other possible reasons stem from differences in the control parameters. KC04 and the present study are closer in physical parameter space, relative to GCHR99. For example, GCHR99 used realistic rotation and magnetic diffusion rates and a relatively strong hyperviscosity, whereas the present study uses slower rotation and uniform viscosity. We have already noted the factor 30 difference between the convective Rossby numbers in these studies. These point to large differences in force balances, and other aspects of the dynamo dynamics that future high-resolution numerical studies might reconcile.

Acknowledgement

We gratefully acknowledge support from CSEDI Grants 0652568, 0652370, and 0652423 from the National Science Foundation.

References

- Alfe, D., Gillan, M., Price, G., 2000. Constraints on the composition of the Earth's core from ab initio calculations. *Nature* 405, 172–175.
- Amit, H., Aubert, J., Hulot, G., Olson, P., 2008. A simple model for mantle-driven flow at the top of Earth's core. *Earth Planets Space* 60, 845–854.
- Aubert, J., Aurnou, J., Wicht, J., 2008a. The magnetic structure of convection-driven numerical dynamos. *Geophys. J. Int.* 172, 945–956.
- Aubert, J., Amit, H., Hulot, G., Olson, P., 2008b. Thermo-chemical wind flows couple Earth's inner core growth to mantle heterogeneity. *Nature* 454, 758–761.
- Braginsky, S., Roberts, P., 1995. Equations governing convection in Earth's core and the geodynamo. *Geophys. Astrophys. Fluid Dyn.* 79, 1–97.
- Burke, K., Steinberger, B., Torsvik, T.H., Smethurst, M.A., 2008. Plume generation zones at the margins of large low shear velocity provinces on the core–mantle boundary. *Earth Planet. Sci. Lett.* 265, 49–60.
- Cande, S., Kent, D., 1995. Revised calibration of the geomagnetic polarity timescale for the late Cretaceous and Cenozoic. *J. Geophys. Res.* 100, 6093–6095.
- Christensen, U.R., et al., 2001. A numerical dynamo benchmark. *Phys. Earth Planet. Int.* 128, 25–34.
- Christensen, U., Aubert, J., 2006. Scaling properties of convection-driven dynamos in rotating spherical shells and application to planetary fields. *Geophys. J. Int.* 166, 97–114.
- Christensen, U., Olson, P., 2003. Secular variation in numerical geodynamo models with lateral variations of boundary heat flow. *Phys. Earth Planet. Int.* 138, 39–54.
- Christensen, U.R., Wicht, J., 2007. Numerical dynamo simulations. In: Olson, P. (Ed.), *Treatise on Geophysics*, vol. 8. Elsevier B.V., pp. 245–282.
- Coe, R.S., Glatzmaier, G.A., 2006. Symmetry and stability of the geomagnetic field. *Geophys. Res. Lett.* 33, L21311.
- Coe, R.S., Hongre, L., Glatzmaier, G.A., 2000. An examination of simulated geomagnetic reversals from a palaeomagnetic perspective. *Philos. Trans. Roy. Soc. Lond.* A358, 1141–1170.
- Coe, R.S., Grommé, C.S., Mankinen, E.A., 1984. Geomagnetic paleointensities of basalts from excursion sequences in lavas on Oahu, Hawaii. *J. Geophys. Res.* 89, 1059–1069.
- Cogne, J.P., Humler, E., 2004. Temporal variations of oceanic spreading and crustal production rates during the last 180 My. *Earth Planet. Sci. Lett.* 227, 427–439.
- Conrad, C.P., Lithgow-Bertelloni, C., 2006. Faster sea floor spreading and lithospheric production during the mid-Cenozoic. *Geology* 35, 29–32.
- Constable, C.G., 2003. Geomagnetic reversals: rates, timescales, preferred paths, statistical models and simulations. In: Jones, C.A., Soward, A.M., Zhang, K. (Eds.), *Earth's Core and Lower Mantle*. Taylor and Francis, London, pp. 77–99.
- Courtilot, V., Besse, J., 1987. Magnetic field reversals, polar wander, and core–mantle coupling. *Science* 237, 1140–1147.
- Courtilot, V., Olson, P., 2007. Mantle plumes link magnetic superchrons to Phanerozoic mass depletion events. *Earth Planet. Sci. Lett.* 260, 495–504.
- Cox, A., Dalrymple, G.B., 1967. Statistical analysis of geomagnetic reversal data and precision of potassium–argon dating. *J. Geophys. Res.* 72, 2603–2611.
- Doell, R.R., Dalrymple, G.B., 1973. Potassium–argon ages and paleomagnetism of Waianae and Koolau volcanic series, Oahu, Hawaii. *Geol. Soc. Am. Bull.* 84, 1217–1241.
- Driscoll, P., Olson, P., 2009a. Polarity reversals in geodynamo models with core evolution. *Earth Planet. Sci. Lett.* 282, 24–33.
- Driscoll, P., Olson, P., 2009b. Effects of buoyancy and rotation on the reversal frequency of gravitationally-driven dynamos. *Geophys. J. Int.*, doi:10.1111/j.1365-246X.2009.04234.x.
- Dziwonski, A.M., 1984. Mapping the lower mantle—determination of lateral heterogeneity in P-velocity up to degree and order-6. *J. Geophys. Res.* 89, 5929–5952.
- Gaffin, S., 1987. Ridge volume dependence on sea floor generation rate and inversion using long-term sea level change. *Am. J. Sci.* 287, 596–611.
- Gallet, Y., Hulot, G., 1997. Stationary and nonstationary behavior within the geomagnetic polarity time scale. *Geophys. Res. Lett.* 24, 1875–1878.
- Glatzmaier, G.A., 1984. Numerical simulations of stellar convective dynamos I. The model and method. *J. Comp. Phys.* 55, 461–484.
- Glatzmaier, G.A., 2002. Dynamo models: how realistic are they? *Annu. Rev. Earth Planet. Sci.* 30, 237–257.
- Glatzmaier, G.A., Coe, R.S., 2007. Magnetic reversals in the core. In: Olson, P. (Ed.), *Treatise on Geophysics*, vol. 8. Elsevier B.V., pp. 283–299, Chapter 9.
- Glatzmaier, G.A., Roberts, P.H., 1996. An anelastic evolutionary geodynamo simulation driven by compositional and thermal convection. *Physica D* 97, 81–94.
- Glatzmaier, G.A., Coe, R.S., Hongre, L., Roberts, P.H., 1999. The role of the Earth's mantle in controlling the frequency of geomagnetic reversals. *Nature* 401, 885–890.
- Gonnermann, H.M., Jellinek, A.M., Richards, M.A., Manga, M., 2004. Modulation of mantle plumes and heat flow at the core–mantle boundary by plate-scale flow: results from laboratory experiments. *Earth Planet. Sci. Lett.* 226, 53–67.
- Gubbins, D., Alfe, D., Masters, G., Price, G., Gillan, M., 2004. Gross thermodynamics of two-component core convection. *Geophys. J. Int.* 157, 1407–1414.
- Gubbins, D., 1999. The distinction between geomagnetic excursions and reversals. *Geophys. J. Int.* 137, 1–4.
- Gubbins, D., Willis, A.P., Sreenivasan, B., 2007. Correlation of Earth's magnetic field with lower mantle thermal and seismic structure. *Phys. Earth Planet. Int.* 162, 256–260.
- Harrison, C.G.A., Ramirez, E., 1975. Areal coverage of spurious reversals of Earth's magnetic field. *J. Geomag. Geoelect.* 27, 139–151.
- Hoffman, K.A., 1981. Paleomagnetic excursions, aborted reversals and transitional fields. *Nature* 294, 67–69.

- Hongre, L., Hulot, G., Khokhlov, A., 1998. An analysis of the geomagnetic field over the past 2000 years. *Phys. Earth Planet. Int.* 106, 311–335.
- Hulot, G., Gallet, Y., 2003. Do superchrons occur without any palaeomagnetic warning? *Earth Planet. Sci. Lett.* 210, 191–201.
- Jones, C.A., 2007. Thermal and compositional convection in the core. In: Olson, P. (Ed.), *Treatise on Geophysics*, vol. 8. Elsevier B.V., pp. 131–186, chapter 4.
- Jonkers, A.R.T., 2007. Discrete scale invariance connects geodynamo timescales. *Geophys. J. Int.* 171, 581–593.
- Kageyama, A., Miyagoshi, T., Sato, T., 2008. Formation of current coils in geodynamo simulations. *Nature* 454, 1106–1109.
- Kutzner, C., Christensen, U.R., 2000. Effects of driving mechanisms in geodynamo models. *Geophys. Res. Lett.* 27, 29–32.
- Kutzner, C., Christensen, U.R., 2002. From stable dipolar to reversing numerical dynamos. *Phys. Earth Planet. Int.* 131, 29–45.
- Kutzner, C., Christensen, U.R., 2004. Simulated geomagnetic reversals and preferred virtual geomagnetic pole paths. *Geophys. J. Int.* 157, 1105–1118.
- Labrosse, S., Jaupart, C., 2006. Thermal evolution of the Earth: Secular changes and fluctuations of plate characteristics. *Earth Planet. Sci. Lett.* 260, 465–481.
- Labrosse, S., Poirier, J.P., Le Mouél, J.L., 2001. The age of the inner core. *Earth Planet. Sci. Lett.* 190, 111–123.
- Langereis, C.G., Dekkers, M.J., DeLange, G.J., Paterne, M., Santvoort, P.J.M., 1997. Magnetostratigraphy and astronomical calibration of the last 1.1 Myr from an eastern Mediterranean piston core and dating of short events in the Brunhes. *Geophys. J. Int.* 129, 75–94.
- Larson, R.L., Olson, P., 1991. Mantle plumes control magnetic reversal frequency. *Earth Planet. Sci. Lett.* 107, 437–447.
- Lay, T., Hernlund, J., Garnero, E., Thorne, M., 2006. A lens of post-perovskite and D'' heat flux beneath the central Pacific. *Science* 314, 1272–1276.
- Lay, T., Hernlund, J., Buffett, B.A., 2008. Core–mantle boundary heat flow. *Nature Geosci.* 1, 25–32.
- Liddicoat, J.C., Coe, R.S., 1979. Mono Lake geomagnetic excursion. *J. Geophys. Res.* 84, 261–271.
- Lowrie, W., Kent, D.V., 2004. Geomagnetic polarity timescales and reversal frequency regimes. In: Channell, J.E.T., Kent, D.V., Lowrie, W., Meert, J. (Eds.), *AGU Geophysical Monograph 145: Timescale of the Paleomagnetic Field*. Amer. Geophys. Un., Washington, DC, pp. 117–129.
- Masters, G., Laske, G., Bolton, H., Dziewonski, A.M., 2000. The relative behavior of shear velocity, bulk sound speed, and compressional velocity in the mantle: implications for chemical and thermal structure. In: Karato, S. (Ed.), *Earth's Deep Interior: Mineral Physics and Tomography From Atomic to Global Scale*. Amer. Geophys. Un., Washington, DC, pp. 66–87.
- McFadden, P.L., Merrill, R.T., 2000. Evolution of the geomagnetic reversal rate since 160 Ma: is the process continuous? *J. Geophys. Res.* 105, 28455–28460.
- Merrill, R.T., McElhinny, M.W., McFadden, P.L., 1996. *Paleomagnetism, the Core, and the Deep Mantle*. Academic Press, San Diego, 531 pp.
- Merrill, R.T., McFadden, P.L., 1994. Geomagnetic field stability: reversal events and excursions. *Earth Planet. Sci. Lett.* 121, 57–69.
- Moffatt, H.K., 1978. *Magnetic Field Generation in Electrically Conducting Fluids*. Cambridge University Press, Cambridge, UK.
- Nakagawa, T., Tackley, P.J., 2004. Effects of thermo-chemical convection on the thermal evolution of the Earth's core. *Earth Planet. Sci. Lett.* 220, 107–119.
- Nakagawa, T., Tackley, P.J., 2008. Lateral variations in CMB heat flux and deep mantle seismic velocity caused by a thermal-chemical phase boundary layer in 3D spherical convection. *Earth Planet. Sci. Lett.* 271, 348–358.
- Pavlov, V.Y., Gallet, Y., 2005. A third superchron during the Early Paleozoic. *Episodes* 28, 1–7.
- Olson, P., Christensen, U.R., 2002. The time-averaged magnetic field in numerical dynamos with non-uniform boundary heat flow. *Geophys. J. Int.* 151, 809–823.
- Olson, P., Driscoll, P., Amit, H., 2009. Dipole collapse and reversal precursors in a numerical dynamo. *Phys. Earth Planet. Int.* 173, 121–140.
- Olson, P., Christensen, U.R., 2006. Dipole moment scaling for convection-driven planetary dynamos. *Earth Planet. Sci. Lett.* 250, 561–571.
- Opdyke, N., Channell, J.E.T., 1996. *Magnetic Stratigraphy*, Int. Geophys. Ser. 64. Academic Press, San Diego, 346 pp.
- Roberts, P.H., 1971. *Dynamo theory*. In: Reid, W.H. (Ed.), *Mathematical Problems in the Geophysical Sciences*. Am. Math. Soc., Providence, RI, pp. 129–206.
- Rotvig, J., 2009. An investigation of reversing numerical dynamos driven by either differential or volumetric heating. *Phys. Earth Planet. Int.* 176, 69–82.
- Ryan, D., Sarson, G., 2007. Are geomagnetic field reversals controlled by turbulence within Earth's core? *Geophys. Res. Lett.* 34, L02307.
- Ryan, P.D., Dewey, J.F., 1997. Continental eclogites and the Wilson Cycle. *J. Geol. Soc.* 154, 437–442.
- Sakuraba, A., Roberts, P.H., 2009. Generation of a strong magnetic field using uniform heat flux at the surface of the core. *Nature Geosci.* 2, 802–805.
- Singer, B.S., Jicha, B.R., Kirby, B.T., Geissman, J.W., Herrero-Bervera, E., 2008. Ar-40/Ar-39 dating links Albuquerque Volcanoes to the Pringle Falls excursion and the Geomagnetic Instability. *Earth Planet. Sci. Lett.* 267, 584–595.
- Stacey, F.D., Davis, P.H., 2008. *Physics of the Earth*, fourth ed. Cambridge University Press, Cambridge, 532 pp.
- Sumita, I., Olson, P., 2002. Rotating thermal convection in a hemispherical shell With heterogeneous boundary heat flux: implications for the Earth's core. *J. Geophys. Res.* 107, doi:10.1029/2001JB000548.
- Takahashi, F., Matsushima, M., Honkura, Y., 2005. Simulations of a quasi-Taylor state geomagnetic field including polarity reversals on the Earth Simulator. *Science* 309, 459–461.
- Takahashi, F., Matsushima, M., Honkura, Y., 2007. A numerical study on magnetic polarity transition in an MHD dynamo model. *Earth Planets Space* 59, 665–673.
- Takahashi, F., Matsushima, M., Honkura, Y., 2008. Scale variability in convection-driven MHD dynamos at low Ekman number. *Phys. Earth Planet. Int.* 167, 168–178.
- Tauxe, L., Yamazaki, T., 2007. Paleointensities. In: Kono, M. (Ed.), *Treatise on Geophysics*, vol. 5. Elsevier B.V., pp. 509–563.
- Trampert, J., Deschamps, F., Resovsky, J., Yuen, D., 2004. Probabilistic tomography maps chemical heterogeneities throughout the lower mantle. *Science* 306, 853–856.
- Valet, J.P., Meynadier, L., Guyodo, Y., 2005. Geomagnetic dipole strength and reversal rate over the past two million years. *Nature* 435, 802–805.
- Valet, J.-P., Plenier, G., Herrero-Bervera, E., 2008. Geomagnetic excursions reflect an aborted polarity state. *Earth Planet. Sci. Lett.*, doi:10.1016/j.epsl.2008.07.056.
- Van der Hilst, R., de Hoop, M.V., Wang, P., Shim, S.-H., Ma, P., Tenorio, L., 2007. Seismostratigraphy and thermal structure of Earth's core–mantle boundary region. *Science* 315, 1379–1381.
- Wicht, J., 2005. Palaeomagnetic interpretation of dynamo simulations. *Geophys. J. Int.* 162, 371–380.
- Wicht, J., Olson, P., 2004. A detailed study of the polarity reversal mechanism in a numerical dynamo model. *Geophys. Geosyst.* 5 (Q03H10), 1–23.
- Wicht, J., Stellmach, S., Harder, H., 2008. Numerical models of the geodynamo: from fundamental Cartesian models to 3D simulations of field reversals. In: Glassmeier, K., Soffel, H., Negendank, J. (Eds.), *Geomagnetic Field Variations: Space–time Structure, Processes, and Effects on System Earth*. Springer, Berlin, Heidelberg, New York, pp. 107–158.
- Willis, A.P., Sreenivasan, B., Gubbins, D., 2007. Thermal core–mantle interaction: exploring regimes for 'locked' dynamo action. *Phys. Earth Planet. Int.* 165, 83–92.
- Yoshida, M., 2008. Mantle convection with longest-wavelength thermal heterogeneity in a 3-D spherical model: degree one or two? *Geophys. Res. Lett.* 35, L23302.
- Zhong, S., Zhang, N., Lib, Z.X., Roberts, J.H., 2007. Supercontinent cycles, true polar wander, and very long wavelength mantle convection. *Earth Planet. Sci. Lett.* 261, 551–564.